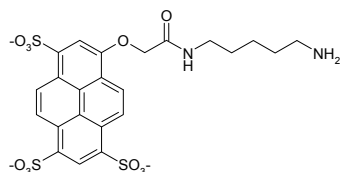# Supplementary Figure 1
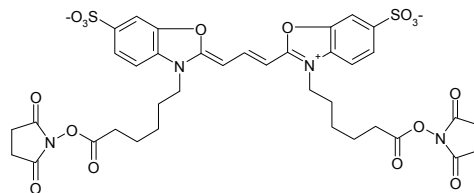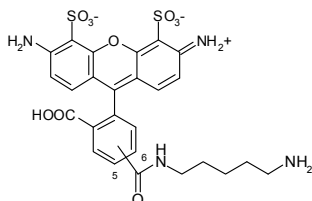
Alexa Fluor 405 cadaverine

Cy2 bis NHS ester

Alexa Fluor 488 cadaverine
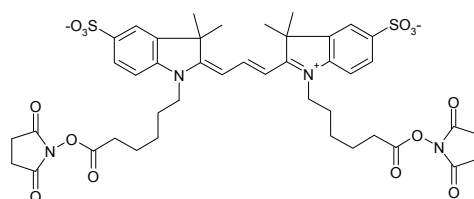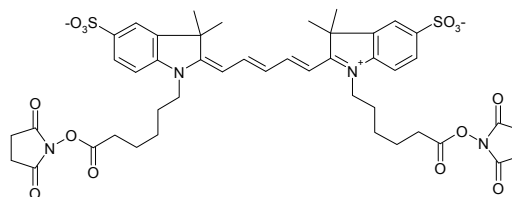
Cy3 bis NHS ester

Cy5 bis NHS ester

Structures of fluorescent dyes used in this article. The structures were obtained from the manufacturer websites (Invitrogen for the Alexa Fluor dyes and GE healthcare for CyDyes). The structures of Alexa Fluor 555 cadaverine and Alexa Fluor 647 cadaverine are not publicly available, but share the same core structures of Cy3 and Cy5, respectively[11].

# Supplementary Figure 2

## a



## b



## c
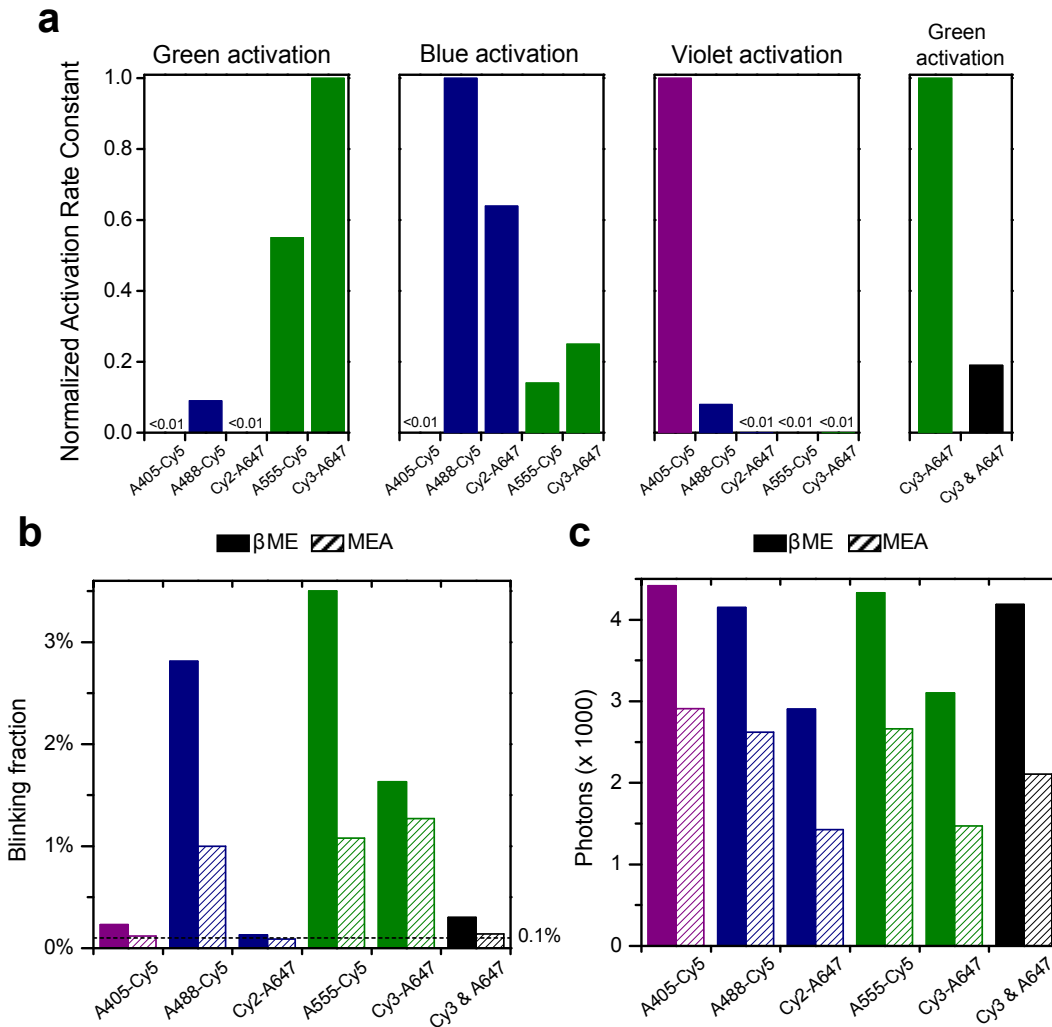


Photoswitching properties of the covalently linked activator-reporter pairs. To mimic the actual STORM imaging conditions, the photoswitching measurements were performed in BS-C-1 cells immunostained with primary antibodies against tubulin and secondary antibodies labeled with the activator-reporter pairs. The A405-Cy5, A488-Cy5, A555-Cy5, Cy2-A647 and Cy3-A647 pairs were tested and these probes are grouped into three colored groups according to the absorption wavelength of the activator portion of the probe: violet probe: A405-Cy5; blue probes: A488-Cy5 and Cy2-A647; and green probes: A555-Cy5 and Cy3-A647. The imaging buffers used are (1) phosphate buffer saline with 100 mM mercaptoethylamine (MEA) at pH 8.5, and an oxygen scavenger system (5% glucose, 0.5 mg/mL glucose oxidase and 40 µg/mL catalase) to reduce photobleaching; or

(2) Similar to (1) except that MEA is replaced with 136 mM β-mercaptoethanol (βME) at pH 8.0. In the following, we refer to buffers (1) and (2) as the MEA and βME buffers, respectively. (**a**) Color specificity of activation measured by comparing the activation rate constants of different dyes. The rate constants were grouped under green (532 nm), blue (460 nm) and violet (405 nm) laser activation. Within each group, the rate constants of all five probes were measured using the same activation laser intensity and the normalized values are shown in each panel. Only results obtained in the βME buffer are shown, and similar results were obtained with the MEA buffer. (**b**) The blinking fraction of the probes defined as the fraction of molecules that were non-specifically activated by the imaging laser at any given time. This fraction was determined by illuminating the sample with a strong imaging laser and measuring the ratio between the ensemble fluorescence intensity after the probes reach the on-off equilibrium and that at the starting point of illumination. (**c**) The number of photons detected from a probe molecule per activation cycle.

# Supplementary Figure 3

**a**



**b**



**c**



**d**
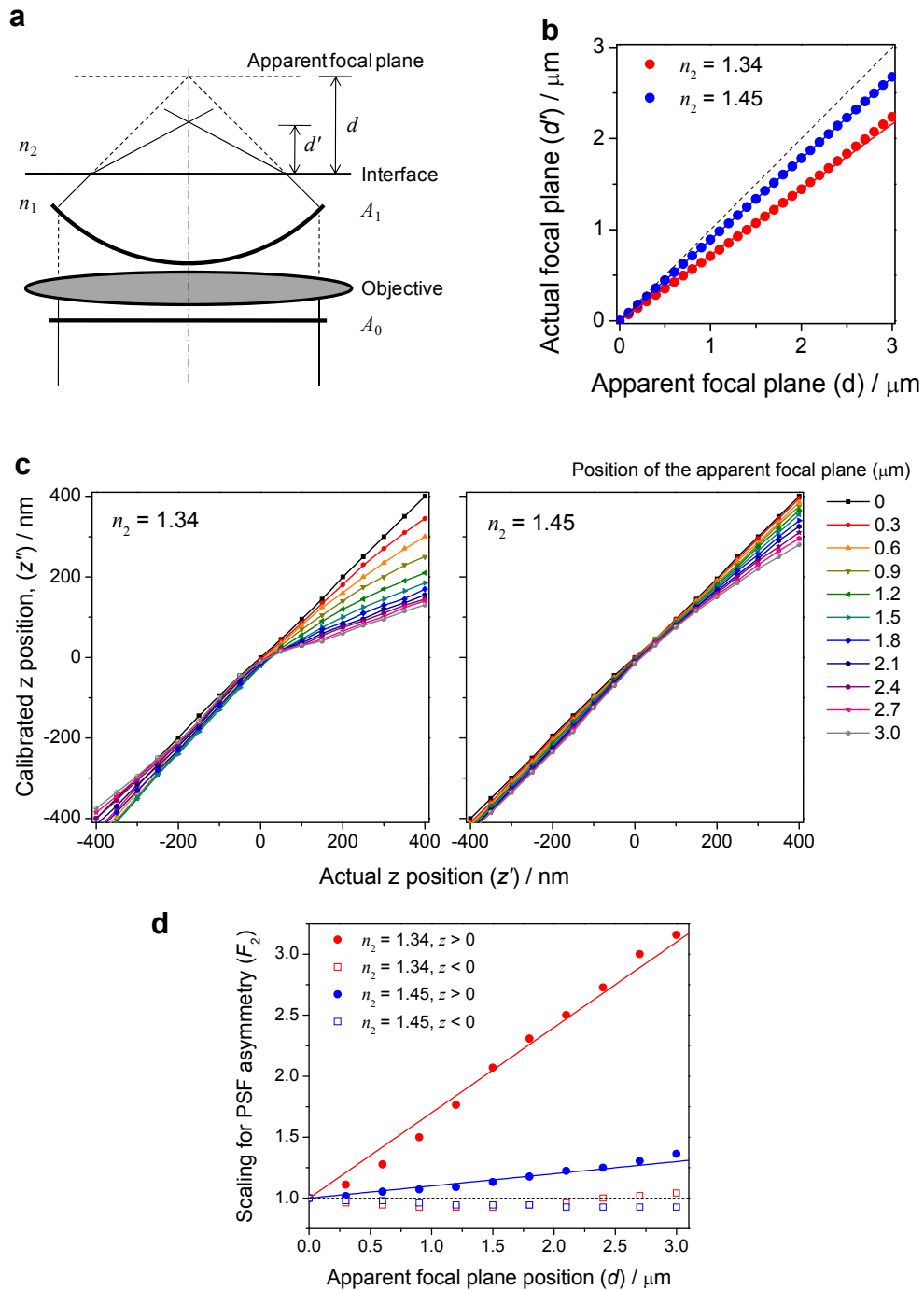


$z$-localization correction for the refractive index mismatch. (**a**) Schematic illustration of how the refraction at the coverglass - imaging medium interface affects light ray propagation. An oil immersion objective was used to index-match the cover glass. Here $A_0$ and $A_1$ indicate the wavefront before and after light propagates through the objective,

respectively, and $n_1$ and $n_2$ indicate the refractive index before and after the interface. The symbols $d$ and $d'$ denote the distance from the apparent and actual focal plane to the interface, respectively. (**b**) The relationship between $d'$ and $d$ determined by numerical simulation for $n_1 = 1.515$ and $n_2 = 1.34$ (red symbols) or $n_2 = 1.45$ (blue symbols). The results are well approximated by straight lines with slopes of 0.72 (red line) and 0.89 (blue line), respectively, except for a very small deviation of the $n_2 = 1.34$ results above 1.5 µm. (**c**) Numerical simulation of the effect of the asymmetry in PSF caused by the spherical aberration from refractive index mismatching. This effect cause an additional shift between the actual $z$ position of a fluorophore ($z'$) measured from the actual focal plane and the apparent $z$ position ($z''$) determined from the calibration curve obtained with the focal plane at the interface. The approximately linear relationship between $z'$ and $z''$ for localizations obtained above or below the focal plane can be described by another scaling factor $F_2^+$ or $F_2^-$, respectively. (**d**) The scaling factor $F_2^+$ (solid symbols) and $F_2^-$ (hollow symbols) to correct for the effect of PSF asymmetry in $z$-localization.

# Supplementary Figure 4
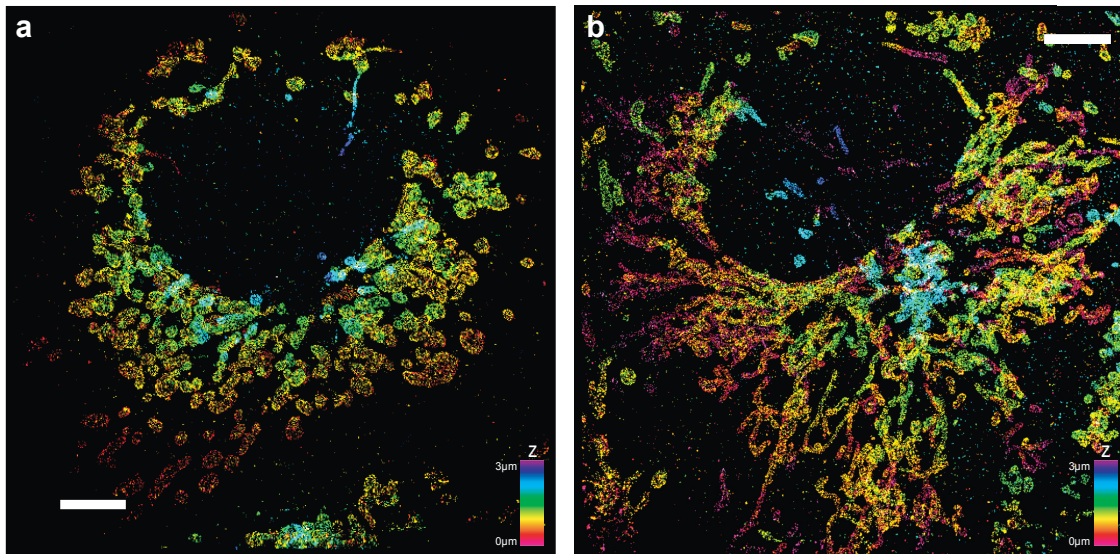


Whole cell STORM images of mitochondria in higher refractive index media. The mitochondria outer membrane protein Tom20 is indirectly immunostained using secondary antibodies labeled with A405-Cy5. The imaging media is based on (**a**) 80% glycerol and 5% glucose and (**b**) 60% sucrose and 5% glucose, both of which have a refractive index of about 1.45.

# Supplementary Figure 5
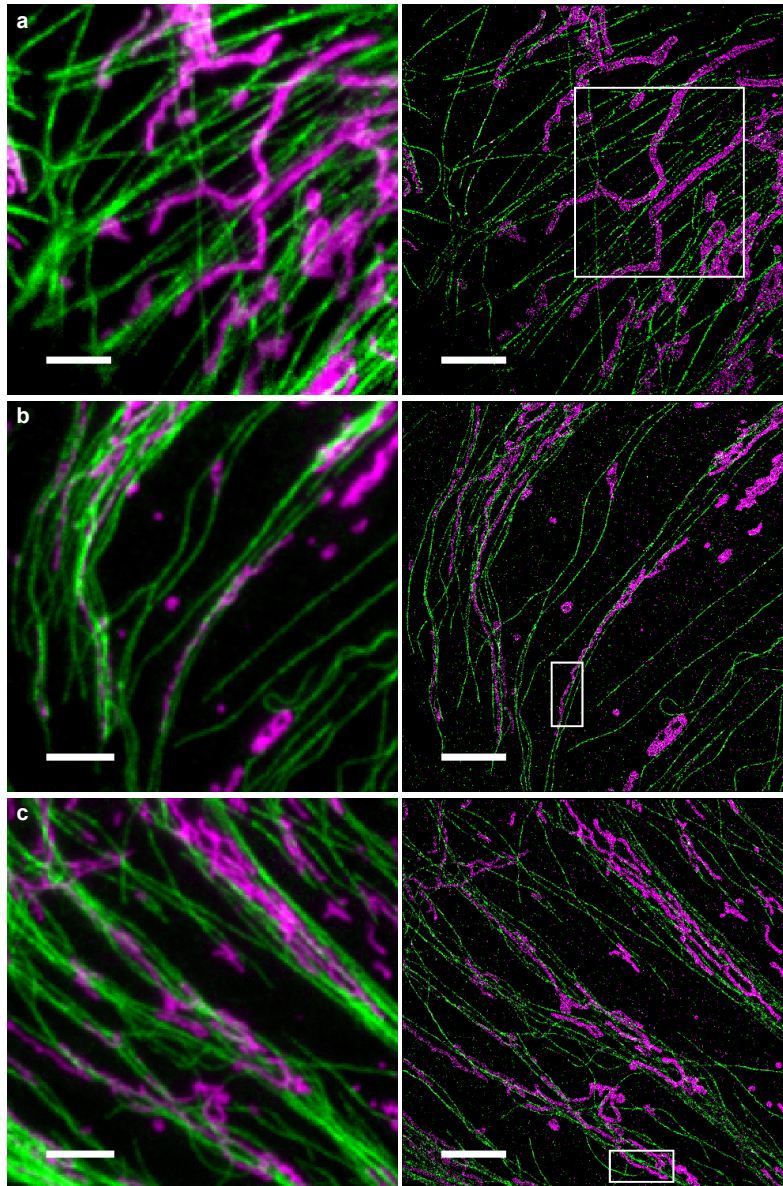


Interactions between tubular mitochondria (magenta) and microtubules (green). Shown here are comparison of conventional fluorescence images (left panels) and their corresponding STORM images (right panels) of three different cells. Mitochondria are labeled with A405-Cy5 tagged secondary antibody. Microtubules are labeled with A488-Cy5 tagged secondary antibody in cell **a**, and A555-Cy5 tagged secondary antibody in cells **b** and **c**. The imaging media is an aqueous buffer with 5% glucose, which has a refractive index of about 1.34. Magnified views of the boxed regions are shown in Figure 4. Scale bars: 5 μm.

# Supplementary Figure 6
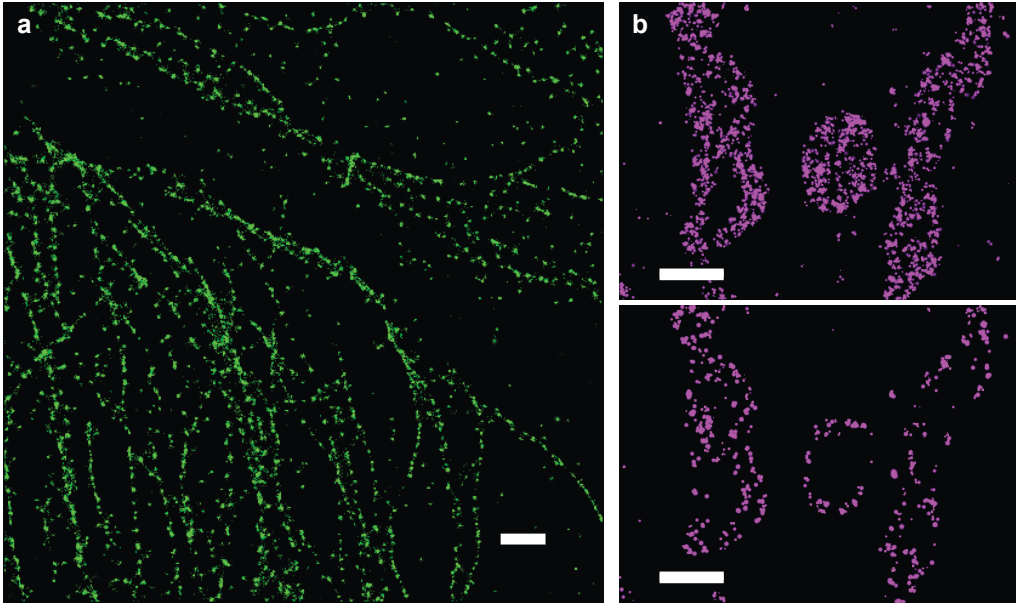


Effects of sample fixation and permeabilization on mitochondria and microtubule structures (**a**) Discontinuous microtubule filaments were observed when BS-C-1 cells were fixed with 2% formaldehyde and 0.1% picric acid. This image contrasts the more continuous microtubules observed in **Figs. 3** and **4** where the cells were fixed with 3% paraformaldehyde and 0.1% glutaraldehyde. More details on the latter fixation and staining protocol can be found in **Supplementary Methods and Discussions**. These results are consistent with previous light microscopy results showing that fixation reagents containing glutaraldehyde preserves the structure of microtubules better[1]. (**b**) Low labeling density of mitochondria outer membrane protein was observed when cells were fixed with 8% formaldehyde, then permeabilized with 0.5% Triton-X100 before immustained for Tom20. The upper panel shows the 2D projection of a 3D STORM image and the lower panel shows a 100 nm thick horizontal section. These images contrast the higher Tom20 label density observed in **Figs. 2-4**, where the cells were permeabilized with 0.2% Triton X100, consistent with the fact that stronger permeablization conditions tend to perturb the distribution of membrane proteins more severely. Scale bars: 1 μm.

# Supplementary Figure 8
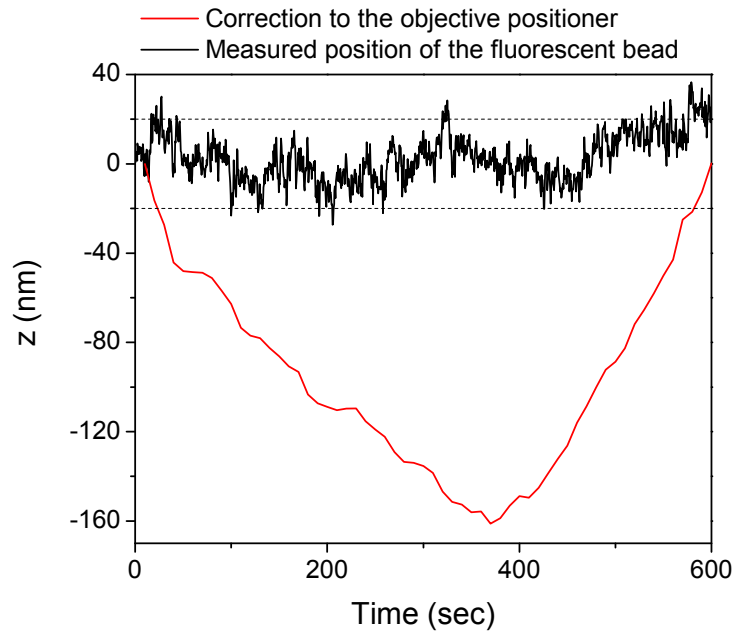


Stability of the microscope stage using the focus lock system. A 20 nm fluorescent bead immobilized on the coverglass surface is continuously imaged for 10 min with the focus lock system engaged. The black curve shows the *z* position of the bead measured using the cylindrical lens system. The red curve shows the change in *z* position of the objective positioner recorded during the experiment. Despite that the stage has drifted for as much as 160 nm in the *z* direction, the position of the bead was kept mostly within ±20 nm from the original position.

# Supplementary Data

## Photoswitching properties of the covalently linked activator-reporter pairs

**The color specificity of activation.** We measured the activation color specificity by comparing the activation rate constants of dye-pairs under different activation wavelengths (**Supplementary Fig. 2a**). Five dye pairs were synthesized and compared. For simplicity: we group these probes into three colored groups according to the absorption wavelength of the activator portion of the probe: A405-Cy5 is referred to as the violet probe: A488-Cy5 and Cy2-A647 are referred to as the blue probes, and A555-Cy5 and Cy3-A647are referred to as the green probes. As is shown in **Supplementary Fig. 2a**, in general, the activation rate constants of the green probes by the green laser are much higher than those of the blue and violet probes. Likewise, the activation rates of the blue probes by the blue laser are much higher than those of the green and violet probes, whereas the activation rate of the violet probe by the violet laser is much higher than those of the blue and green probes, demonstrating highly specific activation in multicolor imaging. False activation of the green probes by the blue (457 nm) laser is the highest, reaching 20% in the case of Cy3-A647. Other false activations are much smaller. The best choice of probes for three-color imaging in terms of activation specificity is the A405-Cy5, A488-Cy5, A555-Cy5 combination, with which the specific activation rates are at least one order of magnitude higher than the false activation rate in all three color channels. Because the color specificity between blue and violet, or green and violet, activations is better than that between blue and green activations, the preferred choices for two color imaging are the blue and violet probes, or the green and violet probes. For example, with A405-Cy5 and A555-Cy5 as the choice of the two-color probes, false activations are almost undetectable. The same is true for the A405-Cy5 and Cy2-A647 combination, or the A405-Cy5 and Cy3-A647 combination. Comparison of the activation rate constant of the covalently linked dye pairs and with that of non-linked activators and reporters separately attached to a common antibody suggest that the former has a much higher activation rate, which can be explained by the short activator-reporter distance in the covalently linked probes and the sharp distance dependence of activation[2].

**The blinking (nonspecific activation) behavior of the probes.** The dark state of cyanine dyes did not exhibit any detectable emission, providing an outstanding contrast ratio between fluorescent and dark state for STORM imaging. Nevertheless, the red (657 nm) imaging laser that switches the probes to the dark state also has a small probability of activating the probes back to the fluorescent state. We refer to this phenomenon as "nonspecific activation" or "blinking". Therefore, each dye will repetitively switch on for brief periods and spend a small fraction of the time overall in the activated state. In other words, after reaching equilibrium, a small fraction of probe molecules will stay at the fluorescent state. We refer to this fraction as the blinking fraction. As both the off-switching and nonspecific activation rate constants depend linearly on the red laser intensity[3], the blinking fraction is independent of the intensity of the imaging laser. While the blinking fraction allows STORM imaging without an activation laser, it can also negatively impact STORM in the following two cases: (1) at high probe density, a number of probes in the field of view will always be on, giving a background signal that reduces localization accuracy; (2) the blinking fraction also results in "colorless" activations and effectively increases crosstalk between different color channels in multicolor imaging. Supplementary Figure 2b shows the blinking fraction of the A405-Cy5, A488-Cy5, A555-Cy5, Cy2-A647 and Cy3-A647 pairs, as well as that of Cy3 and A647 separately attached to a common antibody. Interestingly, the blinking fraction depends on the thiol reagent used in the imaging buffer: Mercaptoethylamine (MEA) containing buffer leads to a lower blinking fraction compared to the βME containing buffer. In this measure, the best choice for two-color imaging is the A405-Cy5 and Cy2-A647 probes, which can have blinking fractions as low as 0.1% in the MEA containing buffer. In the case of three-color imaging, we recommend the use of separate Cy3 and A647 pair as the choice for the third probe.

**The number of photons detected per photoswitching cycle. Supplementary Fig. 2c** lists the number of photons detected from a probe molecule per photoswitching cycle, which ranges from 1500 to 4500 according to the activators and imaging conditions. The number of photons is slightly reduced upon covalent coupling of Cy2 or Cy3 as the activator: for example, the Cy3-A647 linked pair gives 3000 detected photons while Cy3 and A647 separately attached to antibodies give 4000 detected photons in the βME

11

containing buffer. This number is also slightly smaller than previously measured 6000 detected photons[3] due to different buffers conditions used. The number of detected photons directly affects the localization precision[4]. In this particular measure, the best linked dye pairs, which give the highest localization precision, are the A405-Cy5, A488-Cy5 and A555-Cy5 probes.

We note that the optimal choices considering the photon number and those considering the blinking fraction are not necessarily the same. In actual experiments, the proper choice depends on specific experimental requirements, such as the label density. In addition, the fast off-switching rates that yield lower blinking fractions in the MEA buffer also cause a reduction in the numbers of photons detected. The choice between the two buffers thus also depends on specific experimental requirements.

# Supplementary Methods

## 1. Immunostaining of cultured cells

BS-C-1 cells (ATCC) were fixed with 3% paraformaldehyde and 0.1% glutaraldehyde in PBS for 10 min and then reduced with 0.1% sodium borohydride for 7 min. After washing with PBS, the cells were blocked with 3% bovine serum albumin (IgG free) and 0.2% Triton X-100 in PBS for 15 min and stained with rabbit anti-Tom20 (Santa Cruz Biotech, 2 μg/ml ) and/or mouse anti-β-tubulin (TUB2.1, Cytoskeleton, Inc, 2.5 μg/ml ) in blocking buffer for 30 min. The cells were then washed with PBS and stained with the secondary antibodies labeled with an appropriate activator-reporter pair (2 μg/ml) in blocking buffer for 40 min. The cells were then washed with PBS and finally post fixed with 3% paraformaldehyde and 0.1% glutaraldehyde in PBS for 10 min post-staining.

## 2. Microscope setup

STORM measurements were performed on an Olympus IX-71 inverted microscope with an oil immersion objective (100× UPlanSApo, NA 1.4, Olympus). Four laser beams at wavelengths of 657 nm (RCL-200-656, Crystalaser), 532 nm (GCL-200-L, Crystalaser), 460 nm (Sapphire 460-10, Coherent) and 405 nm (CUBE 405-50C, Coherent) were individually controlled by mechanical shutters (Uniblitz LS6T2, Vincent Associates) and used for excitation. The excitation laser was translated off the optical axis of the objective such that the emerging light from the objective arrived at the sample at a high incident angle close to but smaller than the critical angle. The fluorescence emission was collected through the same objective, separated from the lasers with a polychroic mirror (z458/514/647rpc, Chroma), and filtered by a long pass filter (HQ665LP, Chroma) and a band pass filter (HQ710/70m, Chroma) before being imaged on to an EMCCD camera (Ixon DV897DCS-BV, Andor).

# 3. Data analysis

Analysis of the images follows similar methods as described previously using a home written software in C++[3,5]. Briefly, fluorescent images from individual molecules were identified and fit to an elliptical Gaussian function to obtain the centroid position and the widths in the $x$ and $y$ direction. The $z$ position of a molecule was determined by comparing the ellipticity with a predetermined calibration curve of $x$ and $y$ widths as a function of $z$ position. The calibration curve was obtained in a separate experiment by imaging individual A405-Cy5 labeled antibodies on a coverglass while scanning the objective in the $z$ direction. The $z$ position was then corrected for the effect of refractive index mismatch between glass and the imaging medium as described in the next section. Photoactivation events with less than 500 detected photons are excluded in further analyses to ensure the localization precision.

After the 3D localization process, sample drift during acquisition was calculated and subsequently subtracted by correlating STORM images reconstructed from subsets of localizations at different time segments to that from the beginning of the acquisition[5]. The localizations were also corrected for the coma aberration in the imaging optics which causes the measured $x$-$y$ position of a molecule to shift when changing its $z$ position. This effect was measured by computing the correlation function between adjacent 50 nm thin $x$-$y$ sections in STORM images. This correlation function reflects the displacement in the $x$-$y$ direction when changing the $z$ position by 50 nm and the result can be independently verified by tracking the shift in the center positions of surface-immobilizing fluorescent beads as the focal plan is scanned.

For two color imaging, the crosstalk arises from localization points generated by nonspecific activation or false activation with the wrong activation laser. The crosstalk ratios are determined in the regions where mitochondria and microtubules are not overlapping and easily identified. Crosstalk subtraction is then applied uniformly to all localizations in the image using a statistical approach described previously[3]. It is possible that this crosstalk subtraction not only corrects for false activation of the photoswitchable dye pairs, but also corrects for non-specific binding of antibodies. However, the latter effect is small. For example, the color cross talk from the A405-Cy5 channel to the

A555-Cy5 channel calculated from the two color microtubule-mitochondria image is 0.2. To determine the real color crosstalk of the A405-Cy5 probe into A555-Cy5 channel, we also imaged an A405-Cy5 singly labeled sample with alternating 405 nm and 532 nm lasers and determined the crosstalk value to be 0.15, similar to that determined from the two color sample. Though the approach to determine the crosstalk from the two color sample may be limited to samples in which the imaged biostructures have distinct morphologies with substantially non-overlapping regions, the approach of determining cross talk from singly labeled sample is generally applicable to all samples.

In the final STORM image, each photoactivation event is rendered as a normalized Gaussian peak whose width is the larger of its theoretical *x-y* localization precision (calculated from the number of photons detected and the background) and an arbitrary minimum width threshold (at least 12 nm FWHM).

## 4. Correction for refractive index mismatch in $z$ localization

When imaging an aqueous sample using a high numerical aperture (NA) oil immersion objective, the refractive index mismatch between the imaging medium and the coverglass causes the light rays to bend when passing across the interface, affecting the axial localization of individual molecules. Here we analyze these effects quantitatively through numerical calculation of the point spread function (PSF).

To compute the PSF of the microscope objective when imaging through a refractive index mismatched interface, we used the diffraction integral approach[6] previously employed to study the effect of refractive index mismatch in confocal microscopy[7-9]. Similar to the previous work, the excitation PSF (the focal spot of the objective) is used here to approximate the emission PSF (the image of a point source) to simplify calculation. In the diffraction integral approach, the objective converts the planar wavefront of light on the excitation/imaging side, $A_0$, into a spherical wavefront on the sample side, $A_1$ (**Supplementary Fig. 3a**). The PSF, i.e. the spatial distribution of light intensity near the focal spot, is computed by integrating the light propagated from $A_1$ to a given position, $(x, y, z)$. Previous implementations of this approach[7-9] have used a homogeneous light intensity distribution at $A_0$ to describe the focusing of a collimated

beam by the objective. After passing through the objective, this planar wavefront converts into a spherical wavefront with non-uniform intensity that is stronger at the center, whereas isotropic fluorescence emission of point emitter gives a spherical wavefront with uniform intensity. To better approximate this situation, we thus used a homogeneous light intensity distribution at the spherical wavefront of $A_1{}^{10}$.

According to the numerical calculations, within several micrometers from the interface where there is no substantial loss of the signal and the refractive index mismatch affects axial localization mainly in two aspects. One aspect is the focus shift, that is, the distance between the actual focal plane and the interface, $d'$, is smaller than that between the apparent focal plane and the interface, $d$. As seen in the simulated curve of $d'$ as a function of $d$ (**Supplementary Fig. 3b**), this effect is almost linear with a relatively small value of $d$ and the focus shift can be described approximately as

$$d' = Fd$$

where $F$ is the scaling factor. In our case with $n_1 = 1.515$ for glass, $n_2 = 1.34$ for the imaging buffer (5% glucose), NA = 1.40 and the wavelength of light being 680 nm, the calculated value of $F$ is 0.72. With the presence of focus shift, the $z$ position of a fluorophore (relative to the focal plane) read out from the calibration curve needs to be scaled by $F$ because the calibration curve is acquired by scanning the interface where focus shift is absent. Moreover, when imaging a thick sample by acquiring multiple image slices with different focal planes by stepping the objective in the z-direction, the actual focal plane stepping distance also needs to be scaled from the objective stepping distance by a factor of $F$. The focus shift becomes slightly nonlinear as $d$ goes above 1.5 μm. We have applied an additional correction for this nonlinearity by adding $0.05\Delta d$ to $\Delta d'$ for $d > 1.5$ μm. The linear approximations as discussed above matches the actual $d'$ versus $d$ curve with errors much smaller than our $z$-location uncertainty of $60 - 70$ nm for d < 3 μm, which is the imaging depth used in this work. As $d$ goes beyond 3 μm, the actual $d'$ versus $d$ curve needs to be used for correction.

The other effect of refractive index mismatch is the spherical aberration that causes the PSF to become asymmetric in the axial direction. To quantify this effect on $z$-localization, we calculated the $x$ and $y$ widths of the PSF for a fluorophore at a relative position $z'$ from the actual focal plane, $d'$. By comparing the calculated PSF widths with

16

the calibration curves ($x$ and $y$ widths as a function $z$) obtained with the focal plane at the interface, we obtained an apparent $z$-position, $z''$. The relationship between $z''$ and $z'$ is shown in **Supplementary Fig. 3c**. Within a few micrometers to the interface, this relationship is well approximated by another scaling in the axial direction

$$z' = F_2 \, z''$$

except that the scaling factors below $(F_2^-)$ and above $(F_2^+)$ the focal plane are different. The correction below the focal plane ($z' < 0$) is rather small ($0.9 < F_2^- < 1.05$), whereas the value of $F_2^+$ increases nearly linearly with respect to $d'$, changing from $F_2^+ \approx 1$ near the interface to $F_2^+ \approx 3$ at $d = 3$ μm (**Supplementary Fig. 3d**). In our previous 3d STORM work[5] and the two-color imaging experiments here, the effect of PSF asymmetry is small as they were all performed with the objective focal plane close to the interface. In whole cell imaging with some of the focal plane positions far from the interface, however, correction for of PSF asymmetry becomes necessary. Although the average $z$ position can be corrected by the above rescaling factors, the localization precision also rescales with $F_2$. For example, a rescaling factor of $F_2^+ \approx 3$ implies that the localization uncertainty will also be increased by a factor of three. Thus, to ensure the localization precision throughout a thick cellular sample, we chose to accept only localizations below the focal plane where the rescaling factor is very close to unity such that a high localization precision is maintain all across the sample. With this scheme, we stepped the objective in 300 nm intervals (corresponding to an actual $z$-displacement of 216 nm of the focal plane) and localizations within 270 nm (after rescaling) below the focal plane are accepted for the super-resolution image.

Alternatively, the refractive index mismatch can be alleviated using an imaging medium with a higher refractive index. We have demonstrated this approach using two imaging media: 80% glycerol and 5% glucose, or 60% sucrose and 5% glucose, both having a refractive index of $n_2 = 1.45$. The slight mismatch between the medium refractive index and that of the coverglass ($n_1 = 1.515$) is needed for focus locking during imaging. Under these conditions, the focus shift factor $F$ became 0.89 (**Supplementary Fig. 3b**). The correction for the PSF asymmetry also becomes much smaller with $0.9 < |F_2^-| < 1$ below the focal plane and ($1 \leq F_2^+ \leq 1.36$ for $0 \leq d \leq 3$ μm) above the focal plane (**Supplementary Figs. 3c, d**). In this case, the position of the objective was stepped

in 650 nm intervals (corresponding to an actual focal plan displacement of 580 nm). Localizations within 360 nm (after rescaling) above and below the focal plane are accepted.

In both of the above approaches, the stepping interval and the accepted range of localizations were chosen such that the adjacent image slices have a small overlapping region, allowing us to assess the accuracy of the above correction procedures by examine how well the $z$ positions of the same cellular structure determined in adjacent slices are aligned. As discussed in the main text, the alignment error was determined to be about 18 nm, well within out $z$-localization precision. Yet another approach is to use water-immersion objective for imaging in aqueous media, which would essentially eliminate spherical aberration. The advantages and disadvantages of these three approaches are discussed in the main text.

# References

1.  Robinson, R. W. & Snyder J. A. An innovative fixative for cytoskeletal components allows high resolution in colocalization studies using immunofluorescence techniques. *Histochem. Cell Biol.* **122**, 1-5 (2004).

2.  Bates, M., Blosser, T. R. & Zhuang, X. W. Short-range spectroscopic ruler based on a single-molecule optical switch. *Phys. Rev. Lett.* **94**, 108101 (2005).

3.  Bates, M., Huang, B., Dempsey, G. T. & Zhuang, X. W. Multicolor super-resolution imaging with photo-switchable fluorescent probes. *Science* **317**, 1749-1753 (2007).

4.  Thompson, R. E., Larson, D. R. & Webb, W. W. Precise nanometer localization analysis for individual fluorescent probes. *Biophys. J.* **82**, 2775-2783 (2002).

5.  Huang, B., Wang, W. Q., Bates, M. & Zhuang, X. W. Three-dimensional super-resolution imaging by stochastic optical reconstruction microscopy. *Science* **319**, 810-813 (2008).

6.  Richards, B. & Wolf, E. Electromagnetic diffraction in optical systems  2. Structure of the image field in an aplanatic system. *Proc. Royal Soc. London A* **253**, 358-379 (1959).

7.  Hell, S., Reiner, G., Cremer, C. & Stelzer, E. H. K. Aberrations in confocal fluorescence microscopy induced by mismatches in refractive-index. *J. Microsc.* **169**, 391-405 (1993).

8.  Torok, P., Varga, P., Laczik, Z. & Booker, G. R. Electromagnetic diffraction of light focused through a planar interface between materials of mismatched refractive-indexes - an integral representation. *J. Opt. Soc. Am. A* **12**, 325-332 (1995).

9.  Sheppard, C. J. R. & Torok, P. Effects of specimen refractive index on confocal imaging. *J. Microsc.* **185**, 366-374 (1997).

10. Visser, T. D. & Wiersma, S. H. Electromagnetic description of image-formation in confocal fluorescence microscopy. *J. Opt. Soc. Am. A* **11**, 599-608 (1994).

11. Leung, W.Y., Cheung, C.Y. & Yue, S., United States Patent No. 6977305 (2001).